science.sciencemag.org/content/366/6463/346/suppl/DC1

Supplementary Materials for

Hierarchical interlocked orthogonal faulting in the 2019 Ridgecrest earthquake sequence

Zachary E. Ross*, Benjamín Idini, Zhe Jia, Oliver L. Stephenson, Minyan Zhong, Xin Wang, Zhongwen Zhan, Mark Simons, Eric J. Fielding, Sang-Ho Yun, Egill Hauksson, Angelyn W. Moore, Zhen Liu, Jungkyo Jung

*Corresponding author. Email: zross@gps.caltech.edu

Published 18 October 2019, *Science* **366**, 346 (2019)
DOI: 10.1126/science.aaz0109

This PDF file includes:

Materials and Methods

Template matching and seismicity relocation

We used all of the continuous waveform data available for EH and HH channels within 80 km of the Ridgecrest mainshock from the Southern California Earthquake Data Center (doi:10.7909/C3WD3xH1). The data were filtered between 2-15 Hz with a zero phase Butterworth filter. All of the earthquakes listed in the Southern California Seismic Network catalog from 2019/07/04 - 2019/07/25 within 60 km of the mainshock were selected as template events. The template events were relocated individually with a 3D velocity model (*33*) and then pairwise relocated with HypoDD (*34*) using just the phase data from the SCSN. We applied a template matching detection algorithm to the continuous waveform data starting on the first day of the sequence. The procedure closely followed that of Ross et al. (*35*). This resulted in 111,918 detections. Then, we cross-correlated each of these detections with the 100 nearest template events to measure differential times. We used seismograms 1.5 s long, starting 0.25 s before the arrival time. When catalog picks were unavailable we used 1D arrival predictions for selecting the window start time. The maximum source-receiver distance was 80 km, and we only selected event pairs that were within 5 km hypocentral distance. The detections were then relocated with GrowClust (*36*), where we set a minimum correlation threshold of 0.75 and required a minimum of 8 differential times per event pair for relocation. In total 46,512 events were able to be precisely relocated.

To estimate the relative errors on the relocated solutions, we performed a bootstrap analysis by resampling the data 100 times and performing a new inversion for each resample (*36*). For the horizontal and vertical errors, the 90th percentile is 98 m and 340 m, respectively.

Multiple-subevent inversion for the M_w 6.4 and M_w 7.1 earthquakes

Here, we apply a subevent inversion method to estimate rupture process of the Mw 6.4 and Mw 7.1 earthquake sequence. In the method, we treat large earthquake as a series of subevents of varying location, timing and point source focal mechanism. This flexible yet simple source parameterization allows us to constrain first-order rupture complexity of large earthquakes robustly. Mostly important for the complex Ridgecrest earthquakes, the subevent method does not need to assume any particular fault geometry and rupture sequence, while still capturing majority of the moments by inverting regional and teleseismic waveforms.

Subevent methods have been developed since the 1980s (*37–41*). The subevent event method applied here based on a multiple point source method that has been successfully applied on deep earthquakes (*40*, *42*). To resolve the rupture processes of the Ridgecrest events, we incorporate a variety of dataset, including teleseismic P and SH waves and near-field full waveforms for improved spatial and temporal resolutions. The ground phase velocity of the near field Rayleigh and Love waves (~ 3 km/s) are much less than that of the teleseismic body waves (~ 10-20 km/s), making it possible to distinguish rupture on closely located fault segments. We optimize some of the source parameters (locations, centroid times and durations) nonlinearly, while inverting for the rest of the source parameters (moment tensors) linearly. For the nonlinear parameters, we generate Markov chains with a Metropolis-Hasting algorithm, in which the proposal models are generated by sampling through one of the nonlinear parameters while keeping the other nonlinear parameters at their current values (*43*).

In each step of forward calculation, we linearly invert for the subevent moment tensors by extending the approach used by Minson and Dreger (*44*) to multiple subevents. We generate 72 Markov Chains with random first samples, and finally keep the 24 best fitting chains, to

eliminate the dependency of the inversion on the initial values. Subevent moment tensors are constrained to be deviatoric, with no isotropic components. We apply a bounded uniform prior probability density function for all non-linear parameters in the inversion. We also adopt a penalty term to accommodate the moment-duration scaling relationship observed for large earthquakes (*45*) by rejecting models of extremely sharp or flat source time functions. We set the data error to be 10% of the final misfit with the optimal models; the true data errors of seismograms are trivial, but additional prediction errors may be introduced due to nonlinear wave propagation effects (e.g. inaccurate velocity model).

We use teleseismic (epicentral distances from 30 to 90 degrees) P wave records of 33 stations, teleseismic SH wave records of 39 stations, regional (epicentral distances from 50 to 150 km) Rayleigh waves of 31 stations and regional Love waves of 30 stations. The data are selected from all available Global Seismic Network broadband stations and the Southern California Earthquake Data Center strong motion stations for good quality and azimuthal coverage. We remove the instrument response and linear trends of the waveforms, and rotate the two horizontal components to the radial and transverse components. We apply filter bands of 0.01-0.2 Hz for teleseismic body waves and 0.02-0.2 Hz for regional surface waves, and allow time shifts up to 2.0 s for P waves and 5.0 s for SH and surface waves to account for path complexities and picking errors. The calculation of Green's functions is based on the propagator matrix method with plane wave approximation (*37*) for the teleseismic body waves, and the frequency-wavenumber integration method (*46*) for regional surface waves. The source side velocity model is based on a combination of a 4-layer 1D elastic model (Table S1; (*47*)) and iasp91 model (*48*). We start with one subevent and iteratively increase the number of subevents until the main features of the waveform are well fitted and the sum of subevent moments agrees with the long period moment.

The aftershock locations and the InSAR interferograms illuminate the geometry of the faults, which provide important constraints on our subevent models. For the M 6.4 event, we anchor the location of the third subevent by the (arbitrarily chosen) maximum surface offset point on the NE-SW trending conjugate fault observed from the unwrapped interferograms, while the first and second subevents are allowed to move freely in the whole space. A qualitative assessment of the reliability of subevent locations is shown by the ensemble misfits and spanning areas in Fig. S1. For the M 7.1 event, we fix the last subevent at the location where a slip patch is observed from the static slip model, and search for the locations of other subevents along a NW-SE trending plane derived from the surface rupture and aftershocks. The depths of the M 7.1 subevents are searched for between 1-12 km, consistent with the distributions of static slip and aftershocks with depth. The distribution of the Markov Chain ensemble is shown in Fig. S3.

Geodetic Observations—GPS

We used geodetic observations from ground stations of the Global Positioning System (GPS) networks covering the area within 500 km of the earthquakes. Most of the stations are part of the Network of the Americas operated by UNAVCO. We processed GPS data using the JPL processing software GIPSY-OASIS (https://gipsy-oasis.jpl.nasa.gov/) in Precise Point Positioning mode (*49*) using JPL Final orbits and clocks. We estimated daily position time series for all stations. Troposphere delays and gradients were estimated every 300 seconds, and single station ambiguity resolution (*50*) was performed. Mean positions derived from daily positions of 15 days before Mw6.4 and 3 days after Mw7.1 earthquakes are then used to estimate total

coseismic offsets and uncertainties of the earthquake sequence following the approach in Liu et al (*51*).

Geodetic Observations—Satellite Imaging

We used data from two synthetic aperture radar (SAR) satellite systems to extract information about the earthquakes. We used SAR data acquired by the Japan Aerospace Exploration Agency (JAXA) Advanced Land Observation Satellite-2 (ALOS-2) and by the Copernicus Sentinel-1A and -1B satellites operated by the European Space Agency (ESA). We performed three types of analysis of the SAR data to extract information about the static ground displacement during the earthquakes and to map the locations where the fault ruptures reached the surface, including interferometric SAR (InSAR) analysis, interferometric coherence and coherence change used to calculate a Damage Proxy Map (DPM), and SAR pixel matching or pixel offset tracking (described below). We calculated interferograms from the ALOS-2 data and interferograms, DPM, and SAR pixel offsets from the Sentinel-1 data.

The JAXA ALOS-2 SAR uses an L-band (24 cm wavelength) radar and ALOS-2 scenes we used scenes from ascending path 65 that were acquired before (2018-04-16) and after (2019-07-08) the earthquake sequence (Table S2). The pre-event scenes were acquired in stripmap mode (SM3), and the post-event scene was acquired in ScanSAR mode (Figure 3). The stripmap-ScanSAR processing was done using additional modules (*52*) of the InSAR Scientific Computing Environment (ISCE) (*53*). The interferogram was processed with the Shuttle Radar Topography Mission (SRTM) version 3 digital elevation model at 1-arcsecond spacing and had 1 sample in range and 2 lines in azimuth averaged (1 by 2 looks) for the phase unwrapping with SNAPHU (*54*).

The Copernicus Sentinel-1 SAR uses an S-band (5.6 cm wavelength) radar and two tracks cover the Ridgecrest area, ascending track 64 and descending track 71. Scenes we used are listed in Table S2. Sentinel-1 SAR data was acquired in Terrain Observation by Progressive Scans (TOPS) mode (250 km swath) and processed with the ISCE software, using the SRTM elevation data. Interferograms were processed with averaging of 3 range samples and 1 azimuth line to do the phase unwrapping with SNAPHU.

The Sentinel-1 coseismic interferograms extend 5 days and 11 days after the M7.1 earthquake, with the first post-quake acquisition on 10 July for track 64 and 16 July for track 71. This means that the interferograms include a small amount of postseismic deformation. Preliminary analysis of the Sentinel-1 data acquired in the month and a half after the first acquisitions shows that the postseismic deformation rate is moderate, with a maximum rate of about 1 mm/day in the radar line-of-sight. Unless the postseismic deformation rate decreased rapidly in the first few days, then the contribution of postseismic deformation to the coseismic measurements is likely 1 cm or less.

Offset Field Estimation

We estimate offset fields from coregistered Sentinel-1 (S1) SAR amplitude images using a feature tracking algorithm (*55*), which performs dense cross-correlation matching operation to estimate both range and azimuth offsets. We perform feature tracking on one 6-day pair of ascending track 64 (A64 pair) and one 12-day pair of descending track 71 (D71 pair), and apply a median filter that corresponds to a size about 1km x 1km on the obtained offset fields. The spatial resolution of both offset fields is about 200 m x 200 m. Compared with interferograms which also measure displacement in the radar line-of-sight (LOS) direction, range offset fields

are of lower spatial resolution but are able to give measurements at near-fault area where interferograms decorrelate. Besides LOS offsets, offset fields include azimuth offsets measured in the satellite along-track direction, which provide additional constraint to the fault model. Azimuth offset fields is noisier than range offset fields, because azimuth pixel size (14 m) is much larger than range pixel size (2.3 m).

Static Inversion

Data sources: We used GPS data, ALOS-2 ascending, and Sentinel-1 descending coseismic interferograms together with Sentinel-1 azimuth offsets for the static inversion (described above).

Satellite-data downsampling and error models: For computational efficacy, each interferogram is downsampled following a data-resolution approach which attempts to provide locally averaged data at a scale commensurate with the ability of the model to produce variable predictions at that location (*56*). A data covariance matrix is constructed from the standard deviation of the data contained in the blocks emerging from the decimation and a correlation function. The correlation function is derived from the region in the images where the deformation caused by the earthquake is negligible. We compute an empirical covariogram (*56*) over this region from which we extract the correlation function as a function of distance and use this to estimate the full data covariance matrix. Errors in the interferogram phase are largely due to atmospheric water vapor variations that have a strong spatial correlation, so this procedure captures that. Errors in the pixel offsets are due to the local cross-correlation quality and have little effects from atmospheric water vapor.

GPS: We combine the GPS measurements from the M_w 6.4 and M_w 7.1 earthquakes to obtain a measurement consistent with the deformation recovered from SAR. The data covariance is set to be diagonal with an independent variance for each station.

Fault geometry: We manually infer a fault trace from the damage proxy map and the wrapped interferograms. The resulting trace is consistent the complex deformation observed at surface (Fig. 5), but contrasts with the localization of deep seismicity (> 5 km) in an almost straight plane (Fig. 3). As a result, we set a straight fault plane below 5 km depth that follows the deep seismicity and connects to the inferred fault trace using appropriate dipping angles (Fig. 5). We selected a depth-varying patch size consistent with the loss of resolution that geodetic data provides as with increasing depth. Our preferred fault geometry has two segments with subparallel strands. Since proximal parallel strands will have strong trade-offs, we only project one of the subparallel strands throughout the seismogenic zone, limiting the other to the shallowest few kilometers. It is not possible to discriminate which of these two strands accommodate slip at depth but we assume here that the strand with the maximum surface offset corresponds to the dominant fault at depth.

The elastic model and prediction errors: We use the 4-layer 1D elastic model shown in Table S1 for Southern California (*47*). Our imperfect knowledge of the elastic structure may lead to overfitting given resulting errors in our model predictions. We account for prediction errors

through a prediction covariance matrix, C_p, using an approach based on perturbation analysis (*57*). C_p is added to the data covariance matrix, Cd, to form a total misfit covariance, $C_x = C_p + C_d$, which is used in the inverse problem. C_p depends on an assumed covariance for the elastic structure, C_u, here assumed to be diagonal and to correspond to a 10% uncertainty on log(mu), where mu is the shear modulus. (*58*, *59*).

Bayesian sampling: Our results in Fig. 4 represent the mean value of an ensemble of models obtained from sampling the posterior PDF using a modified version of CATMIP, an MCMC-like algorithm (*60*). This procedure is free of any a priori smoothing, a common practice in geophysical inversions that may lead to inconsistent results depending on the arbitrary selection of the smoothing parameters (*60*). The algorithm is embedded into AlTar, a fully parallelized software suite designed for sampling of large inverse problems (*58*, *59*). We select the priors based on the known tectonics of the region. Strike-slip priors are set as bounded uniform distributions between -2 and 12 m oriented in a direction consistent with plate motion (e.g., dextral for the M_w7.1 event and sinistral for the M_w6.4 event). Dip slip priors use a Gaussian prior with 0.5 m as standard deviation and centered at zero.

Garlock creep analysis

Individual interferograms are often contaminated by atmospheric noise, making it hard to extract small signals from them accurately. In order to resolve creep on the Garlock fault, we take all available data for Sentinel 1 (a C-band SAR satellite operated by the European Space Agency) ascending track 64 between June 1st and August 27th and use this to form a time series of ground displacement. We then fit a step function at the time of the earthquake (*61*). The fitted step function will contain coseismic deformation, as well as any motion that has occurred after the earthquake but on timescales much smaller than the time series. The step function fit mitigates atmospheric noise and allows much smaller offset signals to be observed.

This step function is plotted in Figure 6, along with the gradient shading of the step function, allowing us to resolve areas of high gradient in the deformation field. The gradient shading shows a zone of high deformation gradient to the south of the Mw 7.1 mainshock along a section of the Garlock fault approximately 30 km long, with several zones of very sharp deformation gradients. As there was minimal seismicity near the Garlock fault, we infer this deformation to be due to creep on the Garlock fault.

To explore the magnitude of the creep we take profiles across the Garlock where the deformation gradient is sharpest. In order to separate out the motion on the Garlock fault from the long wavelength deformation field due to the earthquake we take profiles across the Garlock fault then remove a polynomial from the profiles. The residuals are plotted in Figure 6.

The overall width of the deformation profile is controlled by the deepest extent of the creep; examining the profiles indicates that creep is not likely to extend below the upper few hundred meters. The gradient of the deformation profile on the fault is determined by the upper extent of the creep, with increasing deformation gradient as creep comes nearer to the surface. Profiles suggest observable surface creep in a few small sections, with much larger zones where creep has not made it to the surface. Profile AA' shows a deformation profile consistent with near surface slip that hasn't broken the surface. A maximum line of sight offset of 20 mm at or very near the surface is observed in profile BB'. Profile CC' shows what appears to be two strands of fault offset, with the largest offset off the main strand of the Garlock.

Burst boundaries in Sentinel-1 interferograms can create apparent discontinuities in the calculated deformation field. One such burst boundary, subparallel to the Garlock fault. is labelled in Figure 6. Care should be taken to distinguish this from an actual tectonic signal.

Thickness (km)	Vs (km/s)	Vp (km/s)	Density (g/cm3)
2.5	2.6	4.34	2.75
3.0	3.5	5.88	2.77
24.5	3.6	6.30	2.90
0.0	4.5	7.74	3.10

Table S1.
The elastic model for Southern California (*47*) used in the computation of static Green´s Functions and prediction errors.

Sensor	Track number (Ascending/Descending)	Preseismic Acquisition Date	Postseismic acquisition date
ALOS-2*	A65	20180416***	20190708
Sentinel-1**	A64	20190704****	20190710
Sentinel-1	D71	20190704	20190716

Table S2

*Advanced Land Orbiting Satellite 2, L-band SAR satellite operated by the Japanese Aerospace Exploration Agency

** C-band SAR satellite operated by the European Space Agency

***ALOS A65 has not been acquired regularly, meaning it was necessary to use a scene taken more than a year earlier

**** Currently Sentinel 1 A64 is acquired every six days (using Sentinel A and B of the constellation) and D71 every 12 days

	Centroid time (s)	Duration (s)	Longitude (°)	Latitude (°)	Depth (km)	Mrr (10^{26} dyne-cm)	Mtt (10^{26} dyne-cm)	Mpp (10^{26} dyne-cm)	Mrt (10^{26} dyne-cm)	Mrp (10^{26} dyne-cm)	Mtp (10^{26} dyne-cm)
E1	2.68	6.42	-117.512	35.724	9.76	0.0025	-0.1831	0.1806	0.0256	0.0344	0.0198
E2	6.24	6.40	-117.510	35.682	5.88	0.0117	-0.2265	0.2147	0.0110	-0.0052	-0.0061
E3	9.05	6.08	-117.552	35.633	4.48	0.0047	-0.2331	0.2284	0.0163	-0.0267	0.0419

Table S3.
Subevent model parameters for the M 6.4 earthquake.

	Centroid time (s)	Duration (s)	Longitude (°)	Latitude (°)	Depth (km)	Mrr (10^{26} dyne-cm)	Mtt (10^{26} dyne-cm)	Mpp (10^{26} dyne-cm)	Mrt (10^{26} dyne-cm)	Mrp (10^{26} dyne-cm)	Mtp (10^{26} dyne-cm)
E1	7.00	9.26	-117.627	35.794	8.20	-0.0316	-2.6543	2.6860	0.1987	0.0525	0.7137
E2	10.28	6.73	-117.572	35.741	4.37	0.0280	-0.8067	0.7787	0.2993	0.2412	0.1385
E3	14.53	4.65	-117.540	35.709	5.86	0.1354	-0.4079	0.2724	0.0307	0.2180	0.0689
E4	19.88	5.70	-117.444	35.616	4.00	0.0388	-0.5098	0.4710	0.0173	0.1461	0.0861

Table S4.
Subevent model parameters for the M 7.1 earthquake.

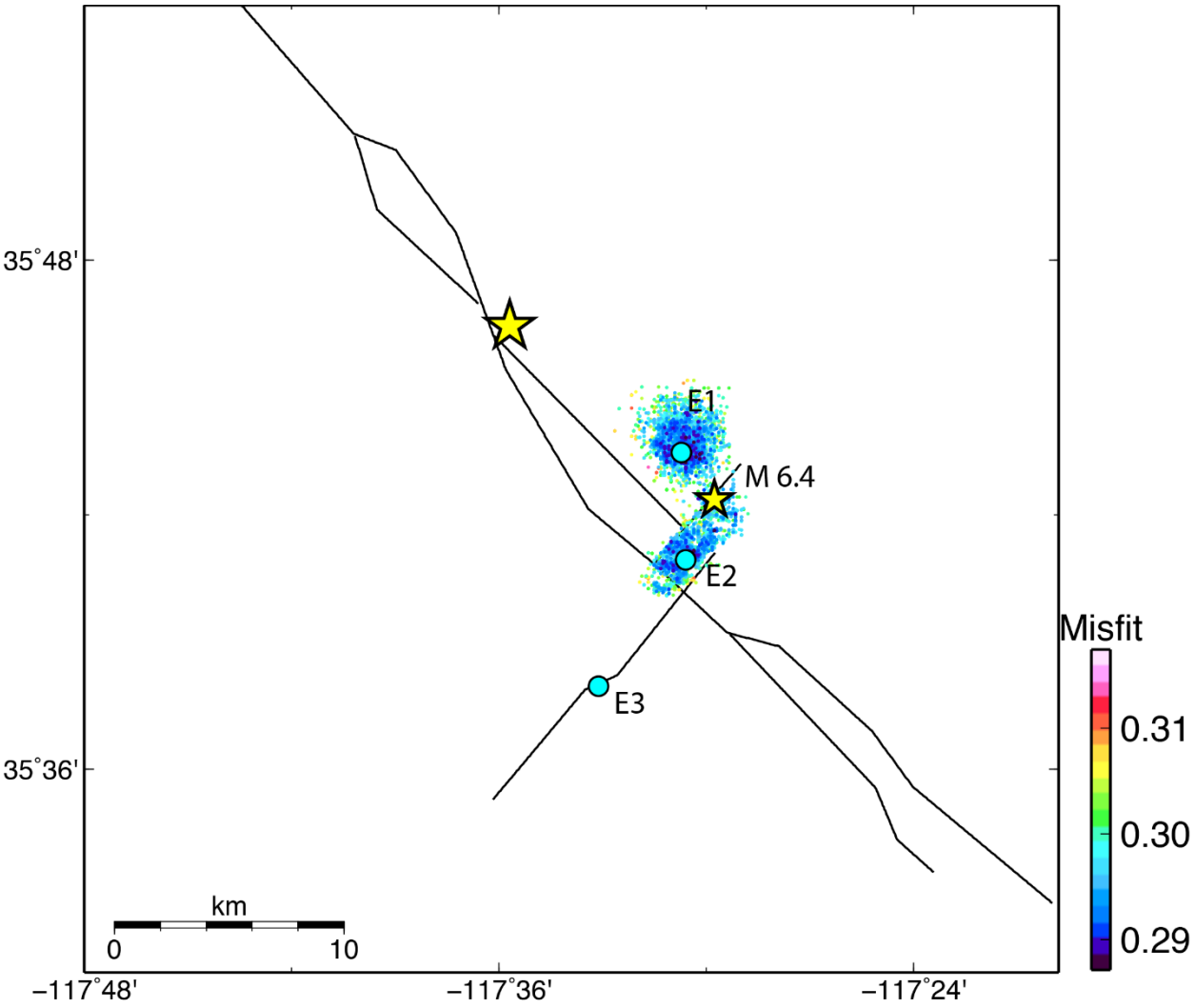

Fig. S1.
Subevent locations of the M 6.4 event revealed by the ensemble of Markov Chain samples. Circles in cyan show the optimal subevent locations corresponding to Fig. 4. The dot clouds indicate Markov Chain samples of different horizontal locations for three subevents. Their color show the corresponding data misfit. Faults are indicated by the black lines. Stars indicate the hypocenters of the M 6.4 and M 7.1 events.

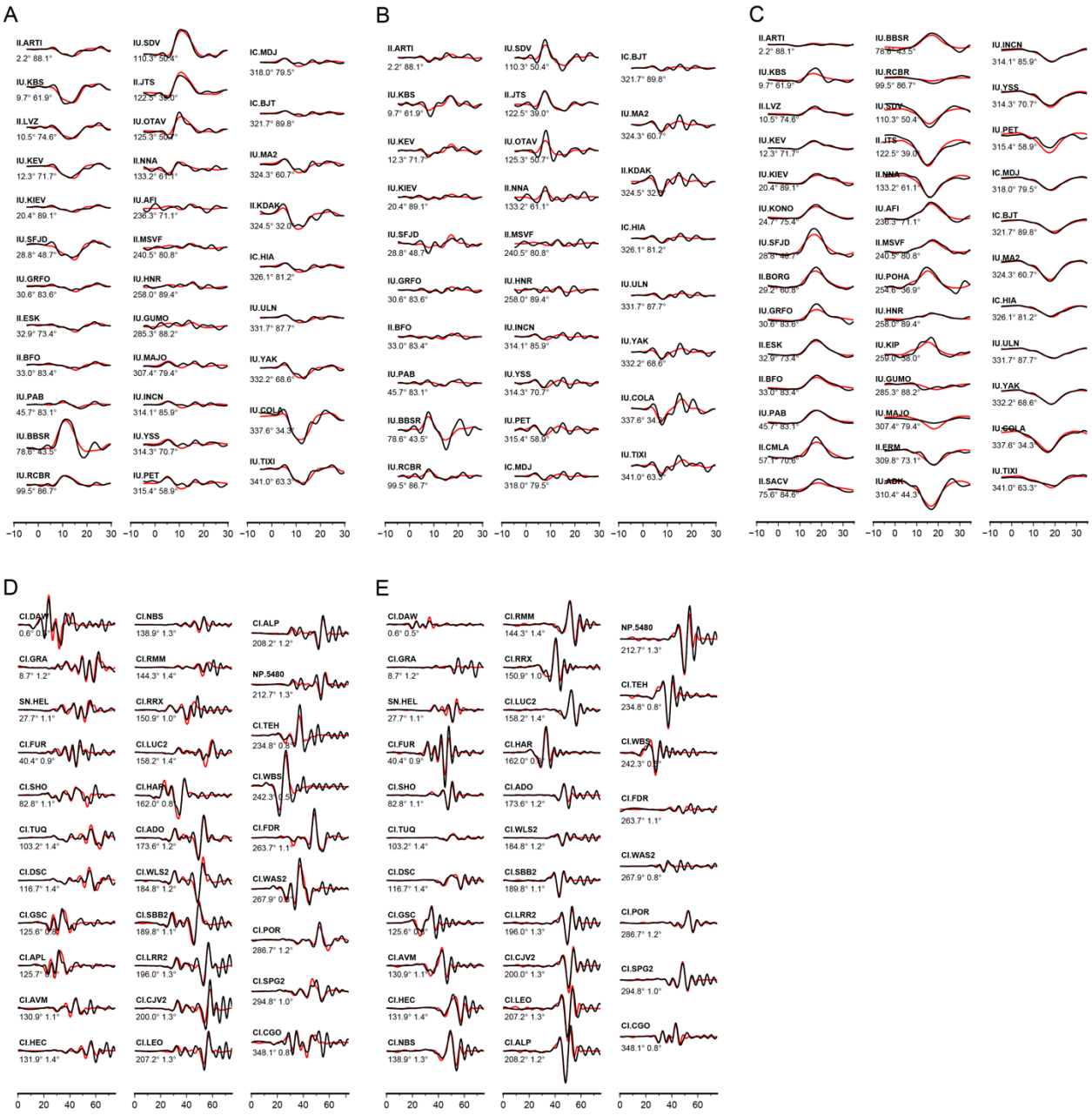

Fig. S2.

Waveform fits for the preferred subevent model of the M 6.4 earthquake. Data and synthetic waveforms are shown in black and red, respectively. The numbers below each trace are the azimuth and distance in degrees. (A) P waves in velocity. (B) P waves in displacement. (C) SH waves in displacement. (D) Rayleigh waves in velocity. Traces are aligned by the event origin time. (E) Love waves in velocity. Traces are aligned by the event origin time.

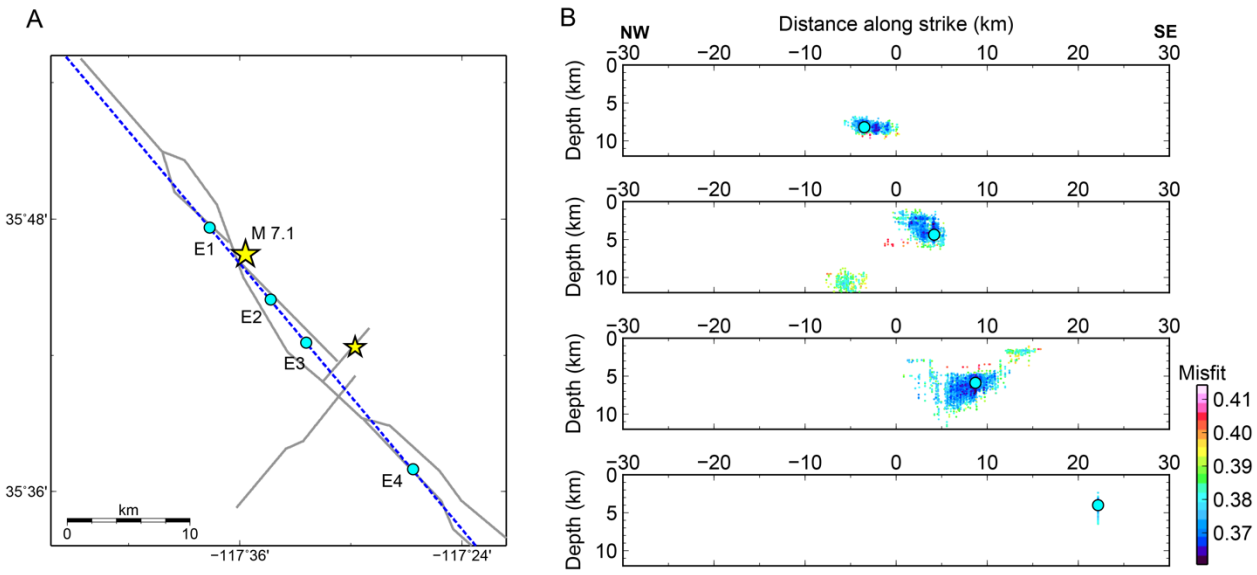

Fig. S3.

Subevent locations of the M 7.1 event. Circles in cyan show the optimal subevent locations corresponding to Fig. 4. (A) A NW-SE trending vertical plane (N40°E) where the subevent locations are searched. The plane is indicated by the dashed blue line. Background gray lines show the faults. Stars indicate the hypocenters of the M 7.1 and M 6.4 events. (B) The ensembles of Markov Chain samples for 4 subevents of the M 7.1 mainshock. Samples (dot clouds) are plotted on the cross-section of the NW-SE trending plane in (A). Their color show the corresponding data misfit.

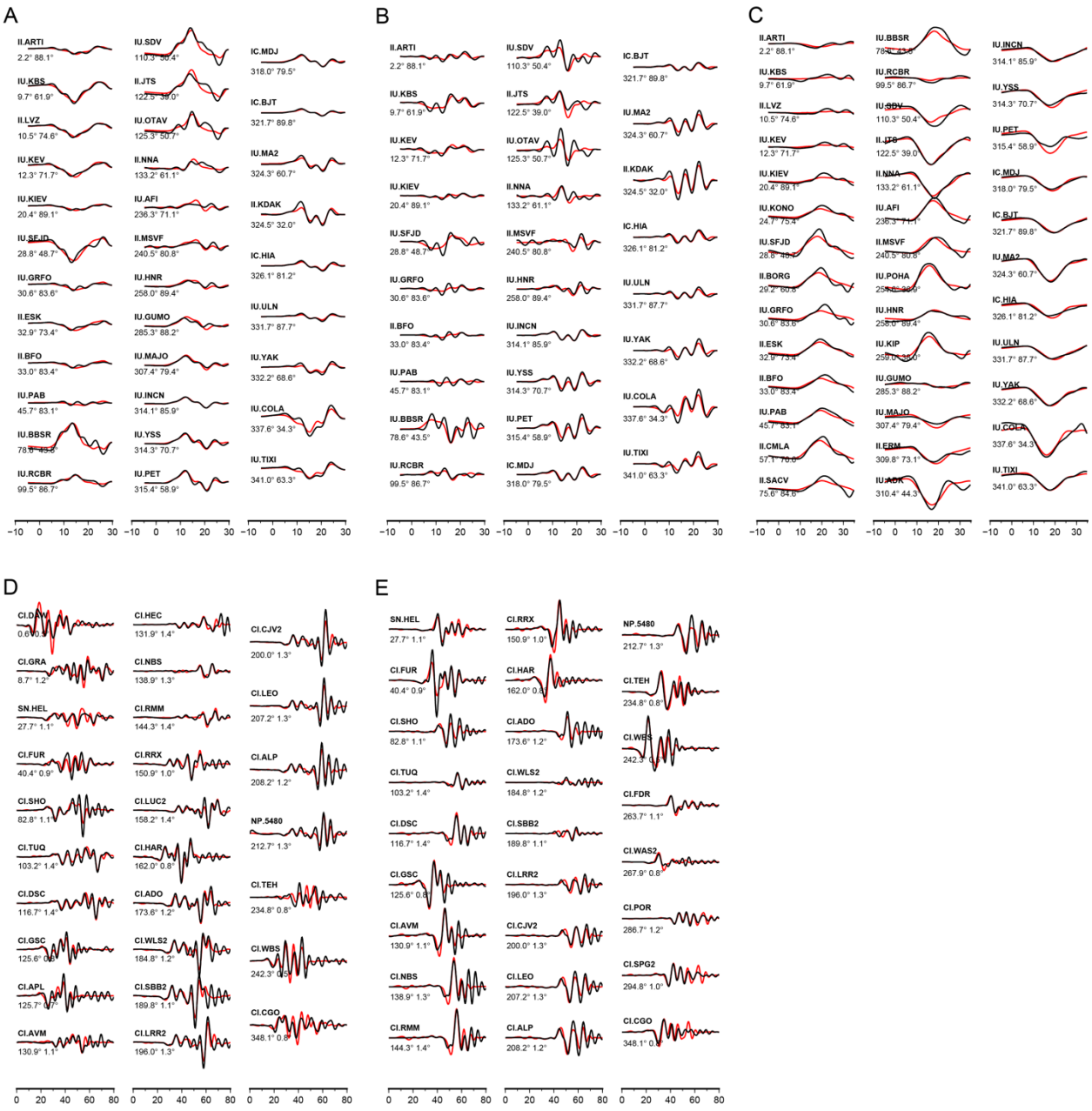

Fig. S4.
Same as Fig. S2 but for the M 7.1 event.

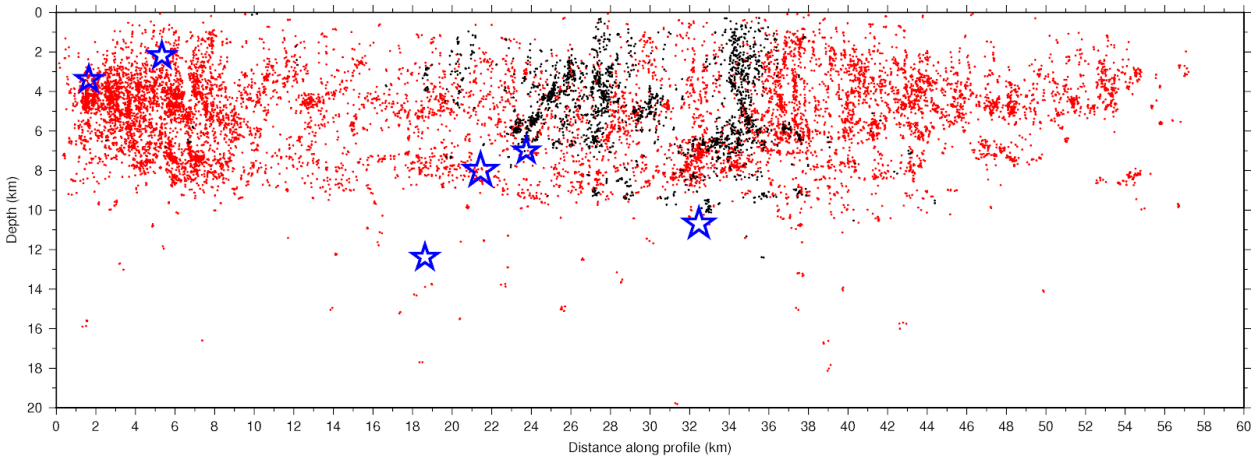

Fig. S5.

Seismicity cross-section along NW-SE fault plane. Earthquakes that occurred prior to the Mw 7.1 mainshock are colored black, while events afterward are colored red. M>5 events are indicated by blue stars.

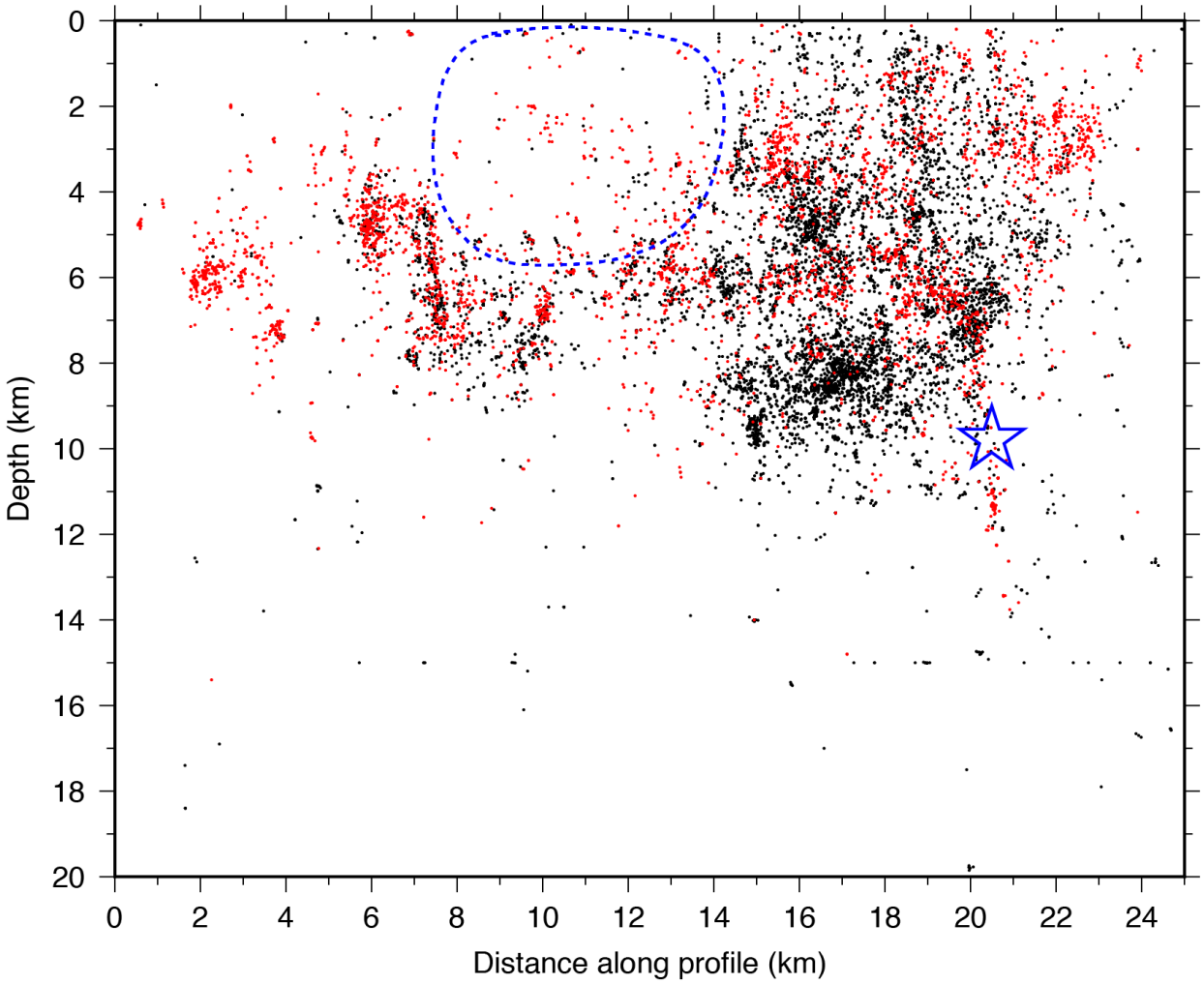

Fig. S6.
Seismicity cross-section along SW-NE fault plane. Earthquakes that occurred prior to the Mw 7.1 mainshock are colored black, while events afterward are colored red. Mw 6.4 event is indicated by blue star. A large gap in seismicity is present with dimensions roughly 6x6 km (blue dashed region). Note the vertical lineations indicating orthogonal faulting throughout the profile.

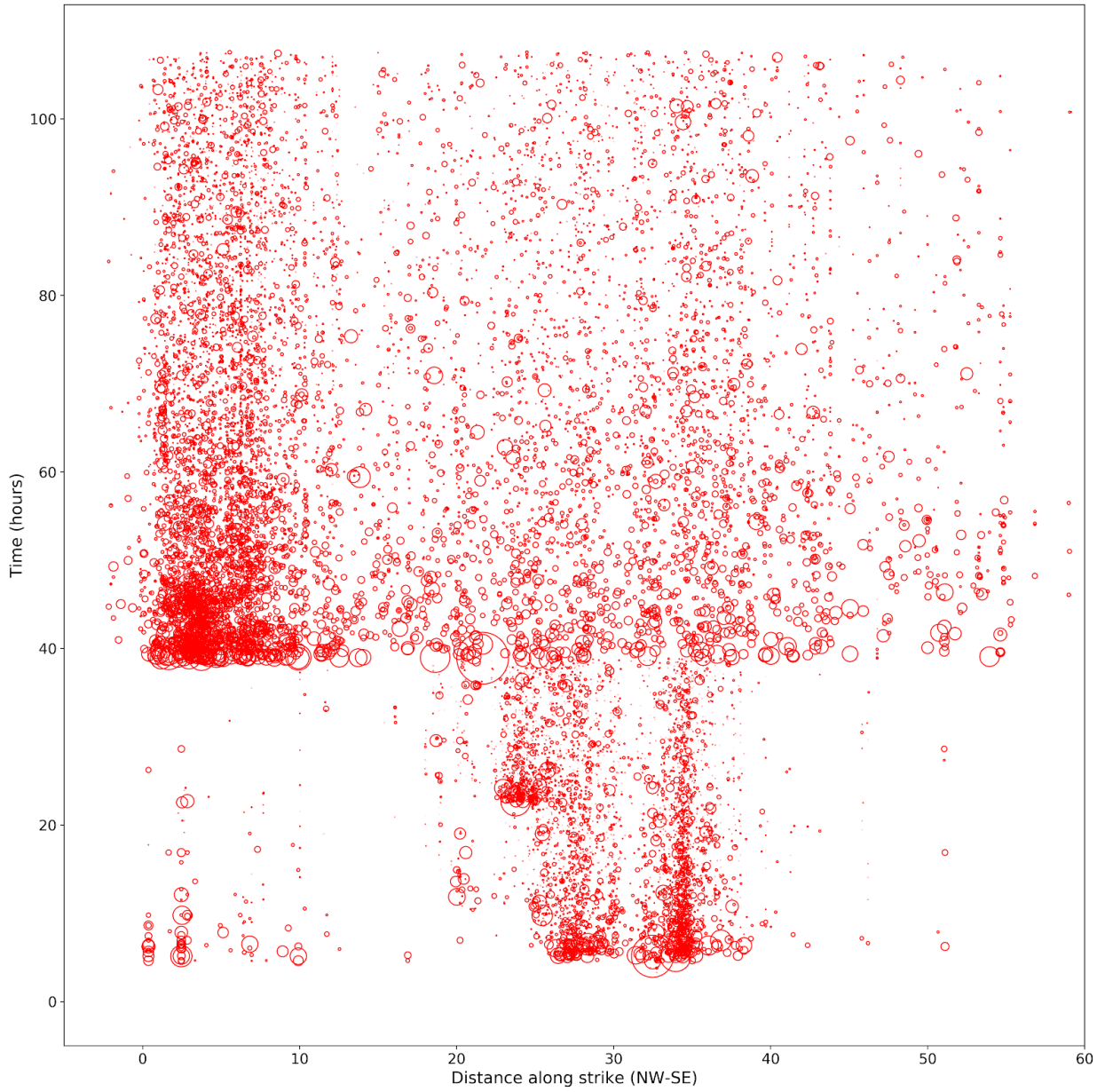

Fig. S7.
Evolution of seismicity projected along strike of M_w 7.1 mainshock. The M_w 6.4 event ruptured a ~6 km segment of the NW fault (Fig. 5) and left behind a gap of aftershocks. The NW edge of the seismic activity expanded over 34 hours through the occurrence of a series of $M > 4$ earthquakes, leading to the nucleation of the M_w 7.1 earthquake.

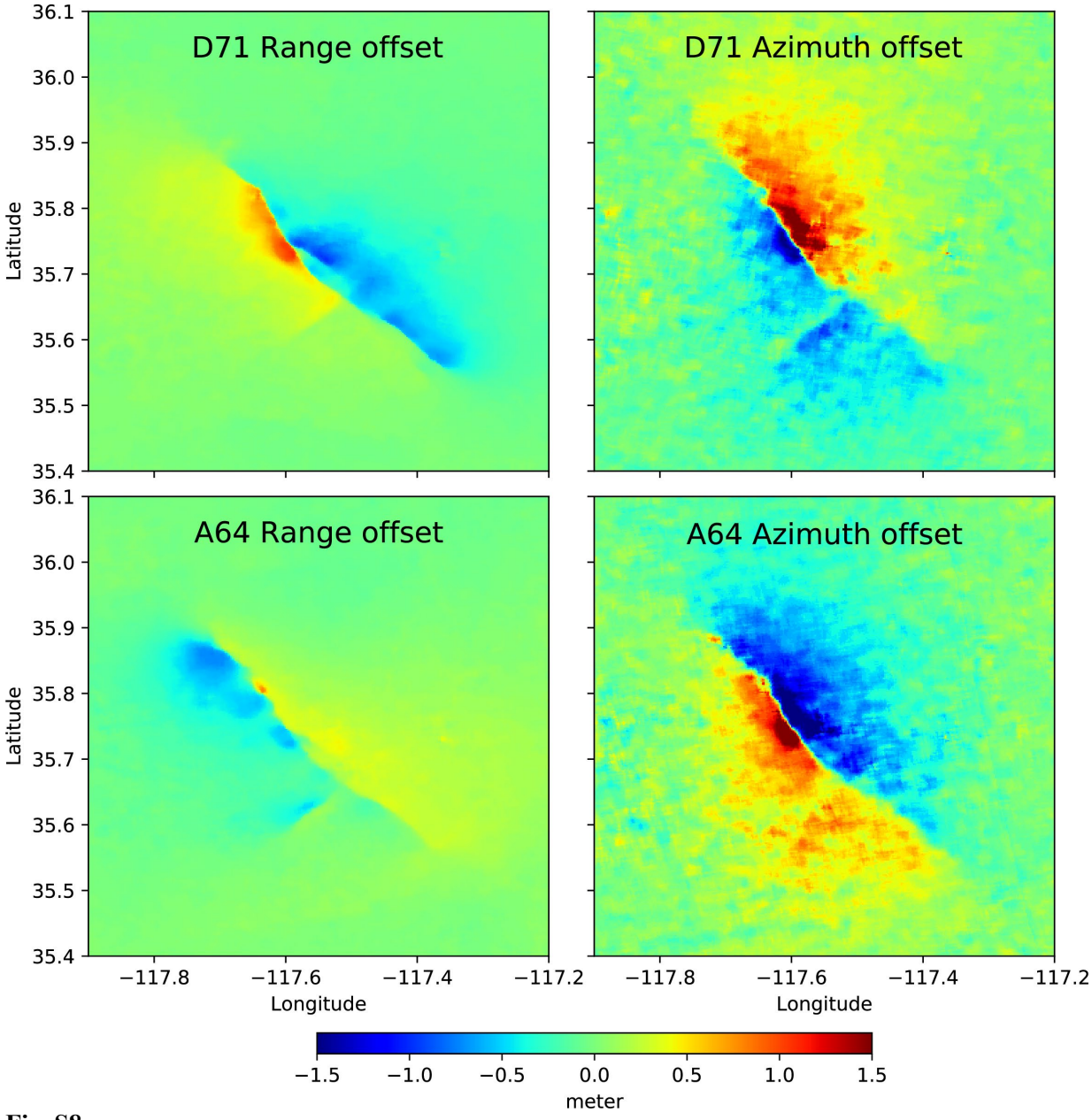

Fig. S8.
Offset fields for Sentinel-1 data.

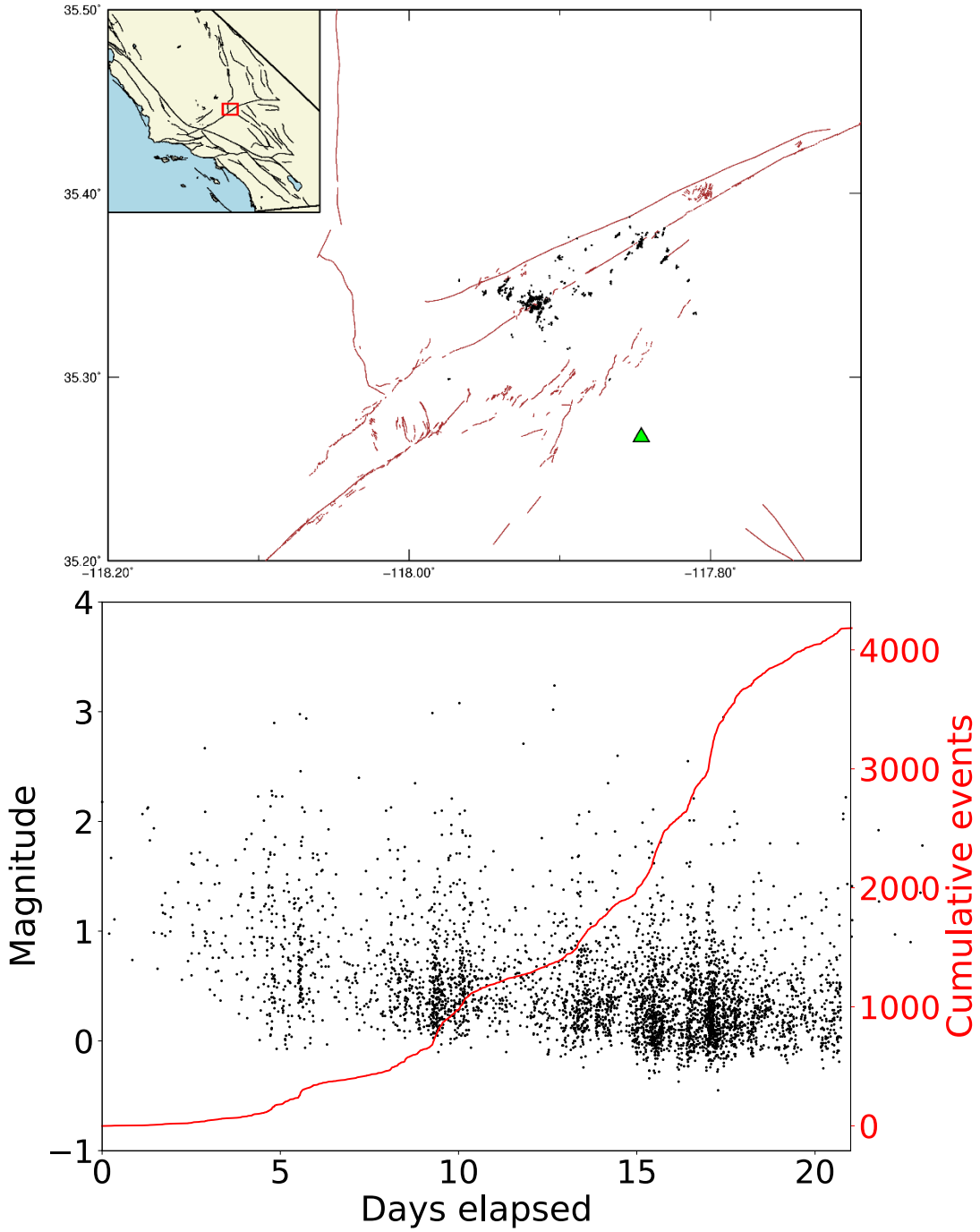

Fig. S9.
Summary of information for the Garlock swarm. Upper panel shows a map view of seismicity. Brown lines indicate faults. Lower panel shows time history of magnitude and event counts.

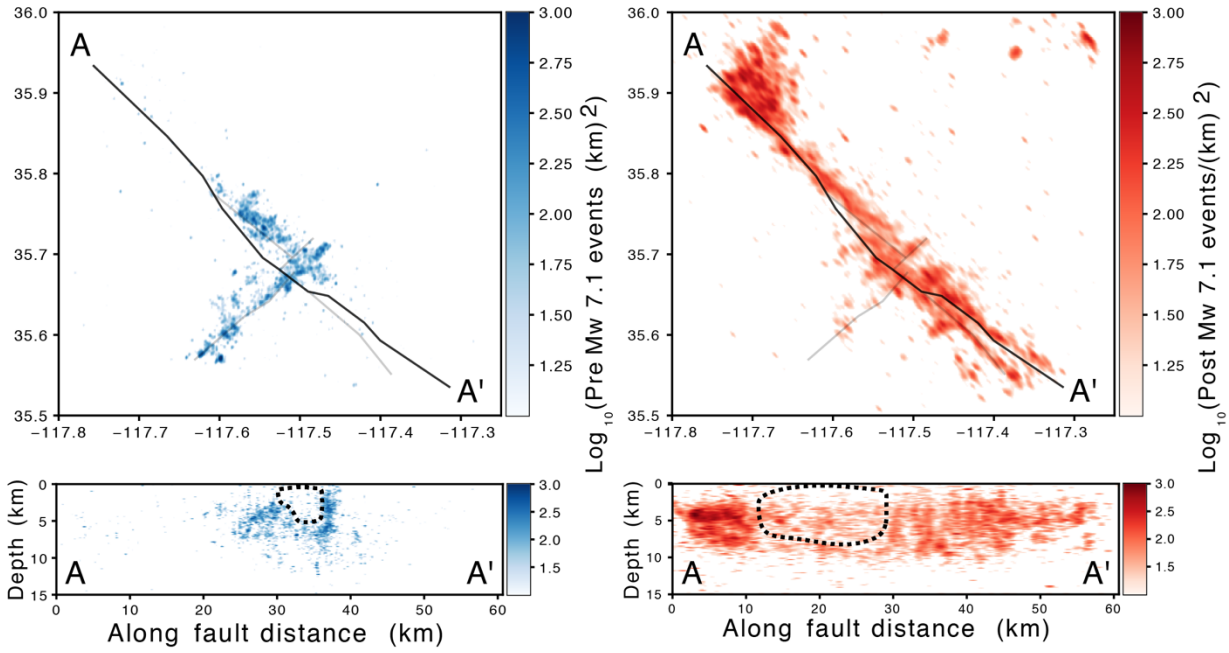

Fig. S10.
The top two panels show log of the seismicity density between the Mw 6.4 and Mw 7.1 (left, blue color scale) and after the Mw 7.1 (right, red color scale) in map view. The lines show a simplified surface fault geometry of the Mw 6.4 and 7.1 earthquakes combined. The main rupture during the Mw 7.1 is represented by the thick line between A and A'. The bottom two panels show log of the seismicity density from the top two panels projected onto the line between A and A' extended vertically down to 15 km, only considering seismicity within 5 km of the surface. Black dashed regions enclose areas of low event density within each seismicity distribution. Again left is between the Mw 6.4 and the Mw 7.1 and right is post Mw 7.1.

Fig. S11.
Decimated data, model predictions, and residuals for the ALOS-2 A65-track interferogram. Red lines show the fault geometry used in the slip model. White stars indicate the location of the M6.4 and M7.1 hypocenters.

Fig. S12.
Decimated data, model predictions, and residuals for the Sentinel-1 D71-track interferogram. The model prediction is the mean model of the ensemble of models produced with AlTar. Red lines show the fault geometry used in the slip model. White stars indicate the location of the M6.4 and M7.1 hypocenters.

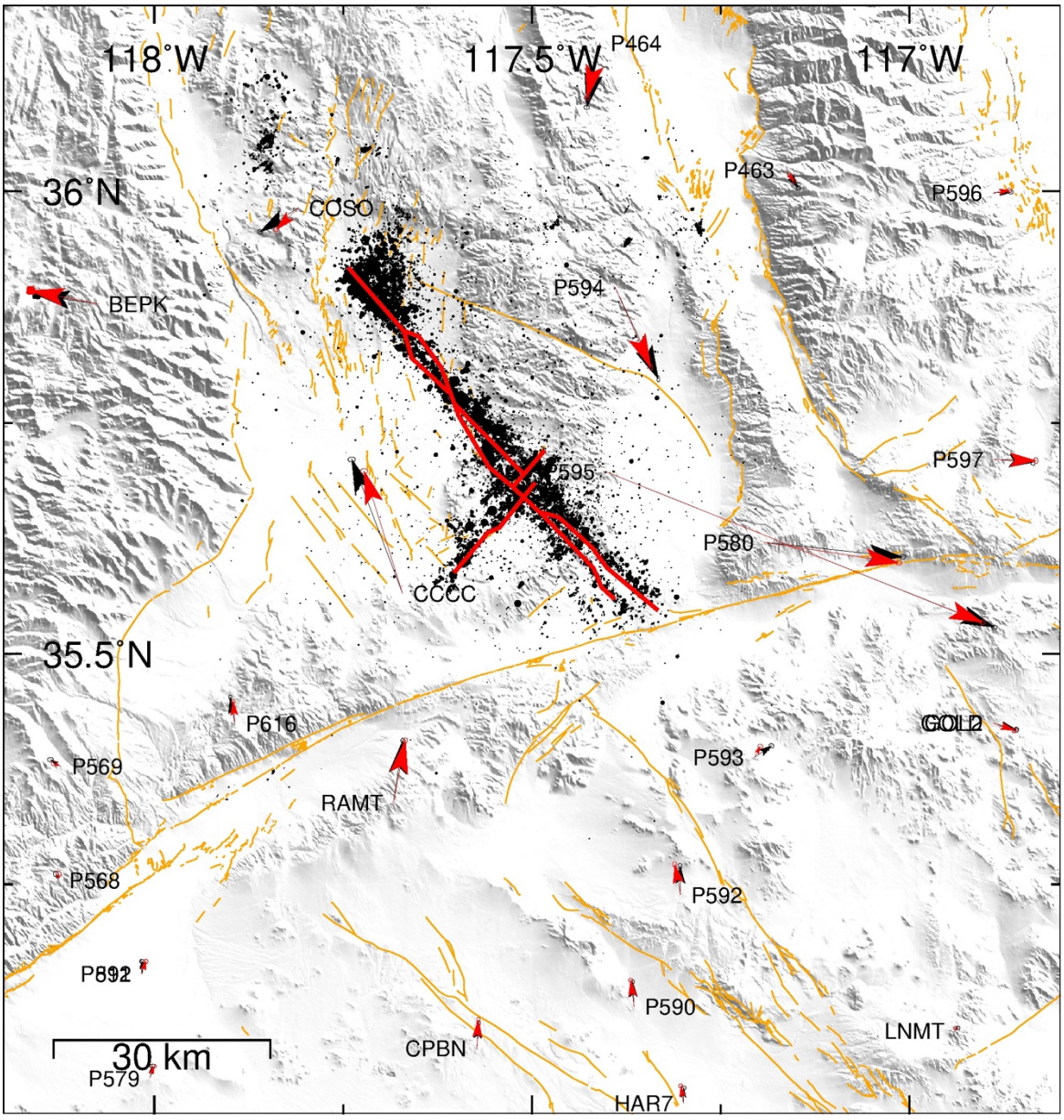

Fig. S13.
GPS data offsets (black arrows) and model predictions (red arrows). The model prediction is the mean model of the ensemble of models produced with AlTar. Red lines show the fault geometry used in the slip model. Black dots indicate the relocated seismicity shown in Fig. 2.

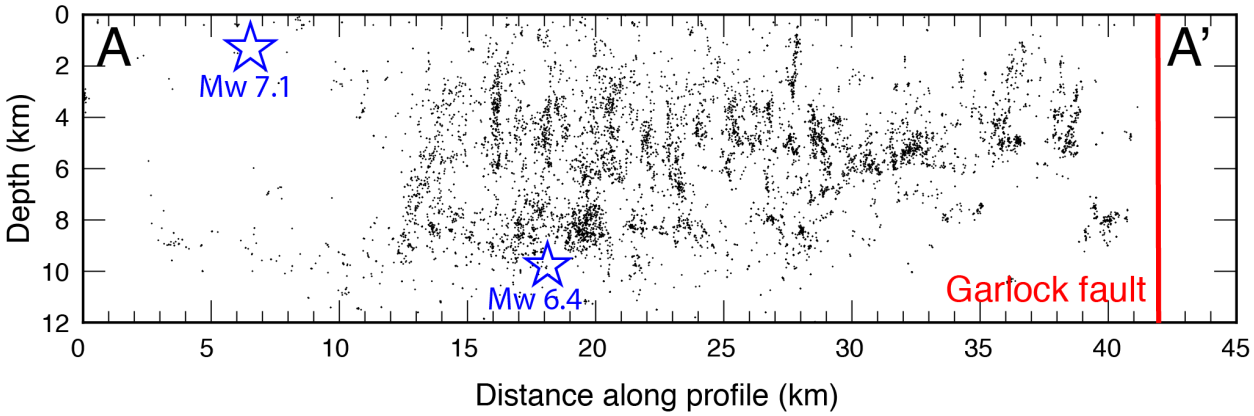

Fig. S14.
Lower panel of Fig. 2 but without interpreted faults drawn.

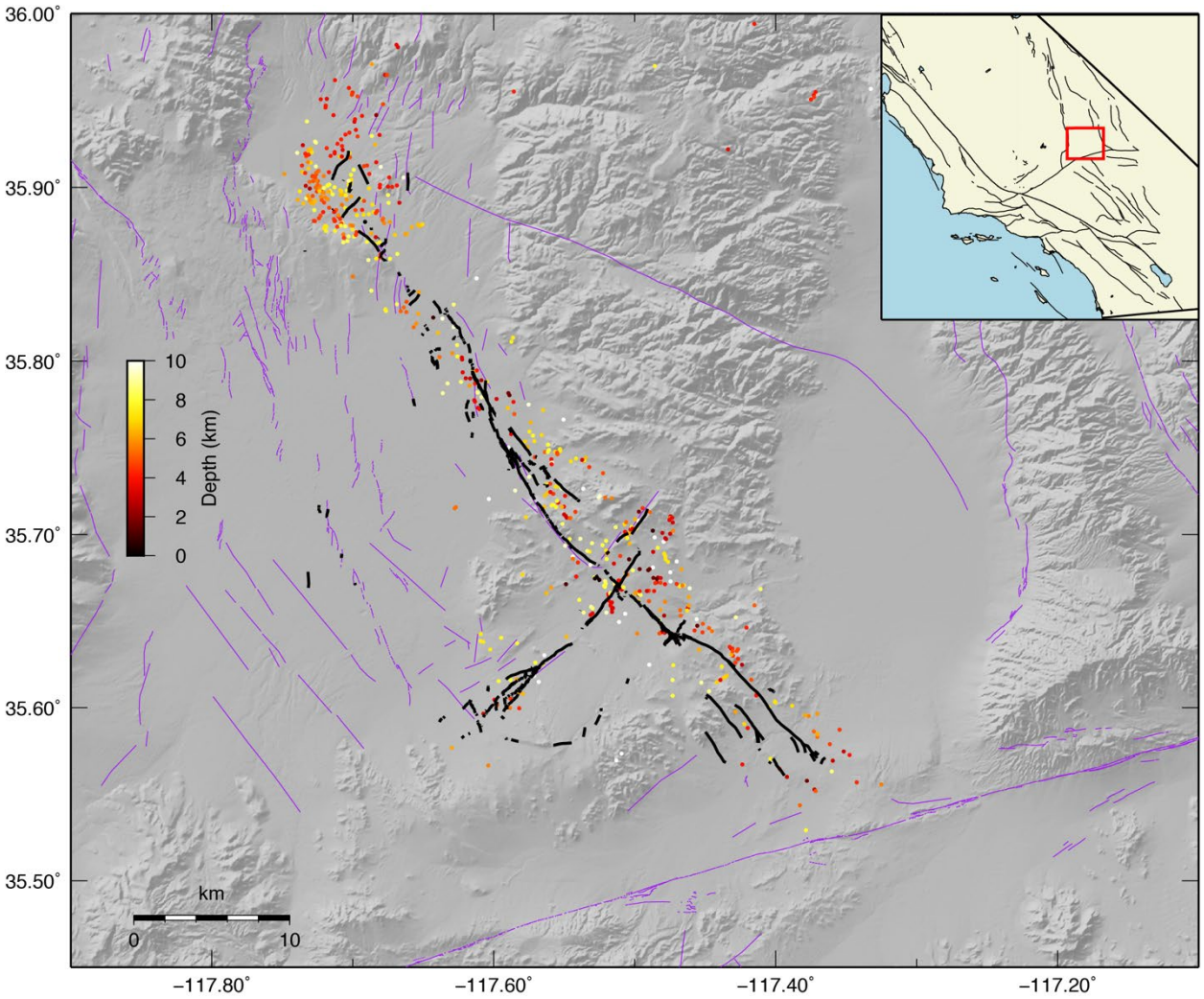

Fig. 15.
Map of M > 3 epicenters. These larger events are associated primarily with the largest faults, and the seismicity pattern is much simpler than that of Fig. 2. This suggests that the largest events are occurring mainly on the most mature fault structures.

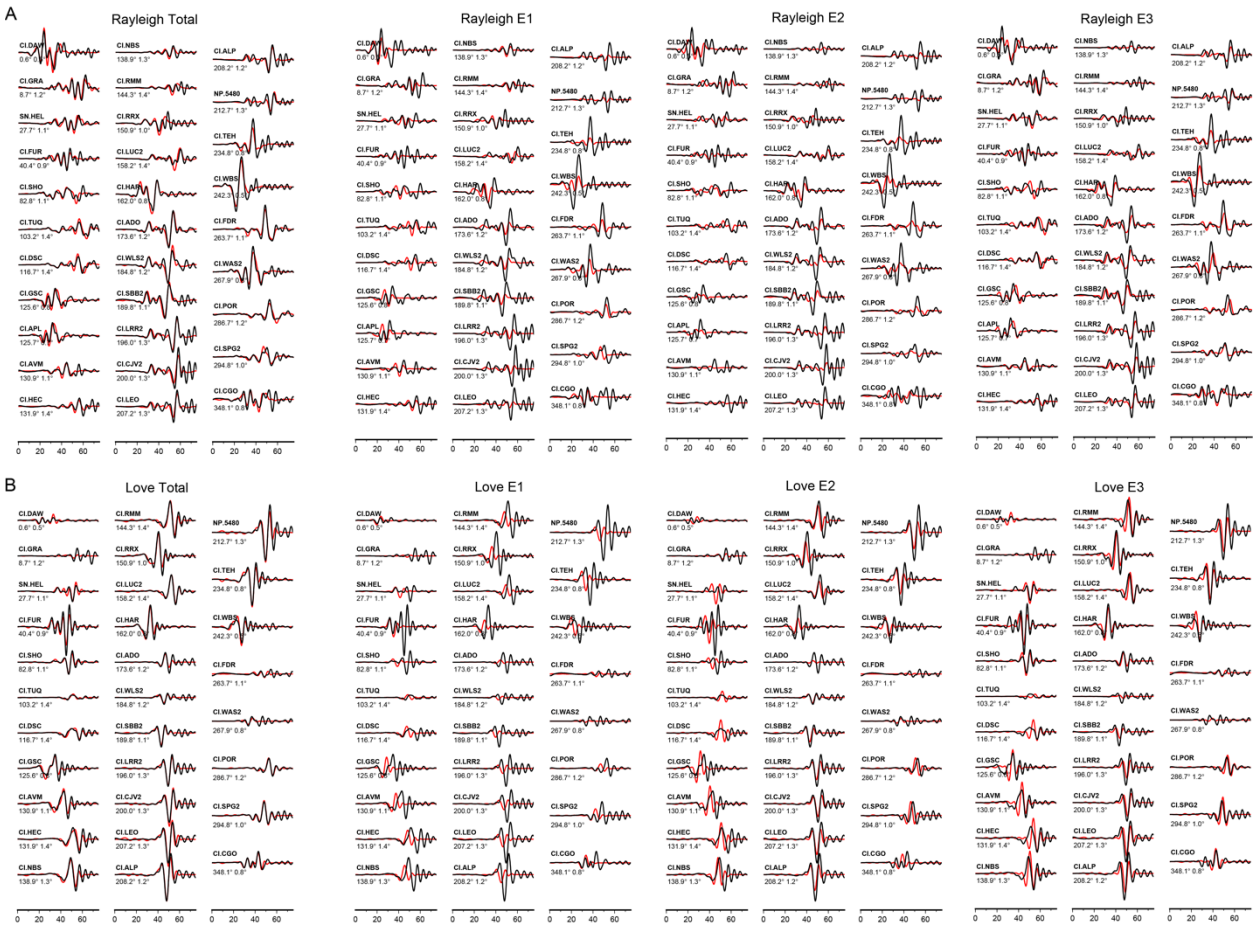

Fig. S16.
Contributions of fittings of (A) Rayleigh waves and (B) Love waves of the M 6.4 event from individual subevents. The waveform records (black) and synthetics (red) are filtered between 0.02-0.2 Hz. The numbers below each trace are the azimuth and distance in degrees.

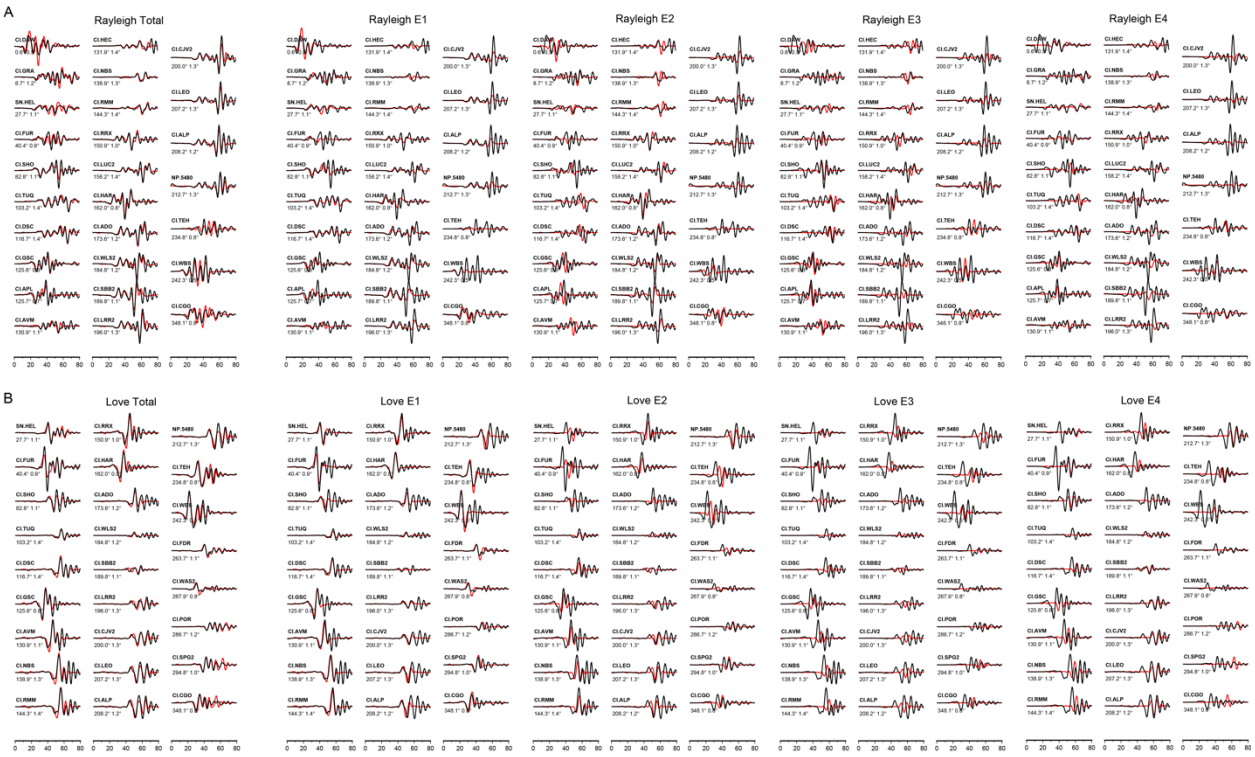

Fig. S17.
Contributions of fittings of (A) Rayleigh waves and (B) Love waves of the M 7.1 event from individual subevents. The waveform records (black) and synthetics (red) are filtered between 0.02-0.2 Hz. The numbers below each trace are the azimuth and distance in degrees.

Fig. S18.
Decimated data, model predictions, and residuals for the Sentinel-1 A64-track azimuth offsets. Red lines show the fault geometry used in the slip model. White stars indicate the location of the M6.4 and M7.1 hypocenters.

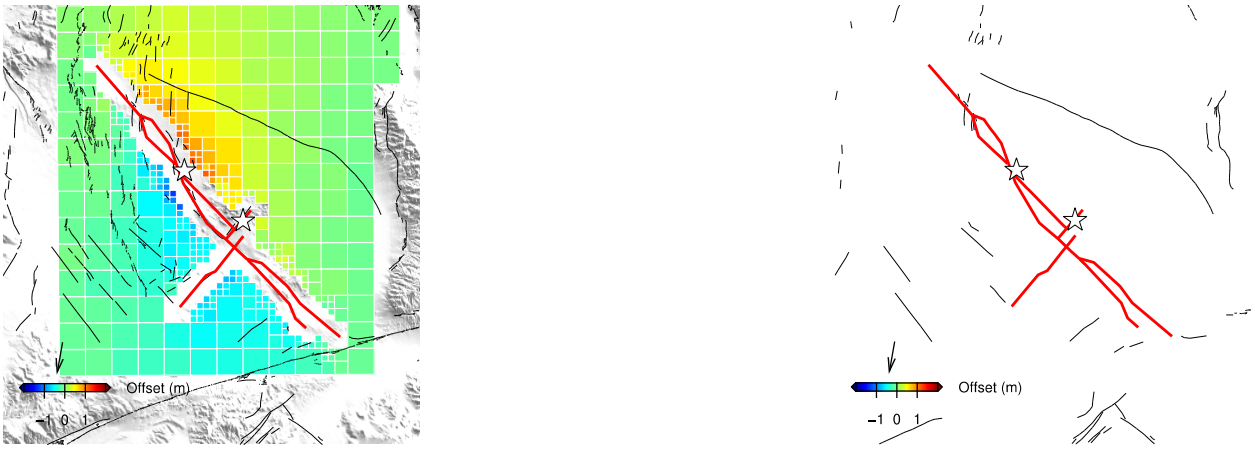

Fig. S19.
Decimated data, model predictions, and residuals for the Sentinel-1 D71-track azimuth offsets. Red lines show the fault geometry used in the slip model. White stars indicate the location of the M6.4 and M7.1 hypocenters.

References and Notes

1. K. Sieh, L. Jones, E. Hauksson, K. Hudnut, D. Eberhart-Phillips, T. Heaton, S. Hough, K. Hutton, H. Kanamori, A. Lilje, S. Lindvall, S. F. McGill, J. Mori, C. Rubin, J. A. Spotila, J. Stock, H. K. Thio, J. Treiman, B. Wernicke, J. Zachariasen, Near-field investigations of the Landers earthquake sequence, April to July 1992. *Science* **260**, 171–176 (1993). doi:10.1126/science.260.5105.171 Medline

2. M. Simons, Y. Fialko, L. Rivera, Coseismic Deformation from the 1999 Mw 7.1 Hector Mine, California, Earthquake as Inferred from InSAR and GPS Observations. *Bull. Seismol. Soc. Am.* **92**, 1390–1402 (2002). doi:10.1785/0120000933

3. D. Eberhart-Phillips, P. J. Haeussler, J. T. Freymueller, A. D. Frankel, C. M. Rubin, P. Craw, N. A. Ratchkovski, G. Anderson, G. A. Carver, A. J. Crone, T. E. Dawson, H. Fletcher, R. Hansen, E. L. Harp, R. A. Harris, D. P. Hill, S. Hreinsdóttir, R. W. Jibson, L. M. Jones, R. Kayen, D. K. Keefer, C. F. Larsen, S. C. Moran, S. F. Personius, G. Plafker, B. Sherrod, K. Sieh, N. Sitar, W. K. Wallace, The 2002 Denali fault earthquake, Alaska: A large magnitude, slip-partitioned event. *Science* **300**, 1113–1118 (2003). doi:10.1126/science.1082703 Medline

4. S. J. Wei, E. Fielding, S. Leprince, A. Sladen, J. P. Avouac, D. Helmberger, E. Hauksson, R. S. Chu, M. Simons, K. Hudnut, T. Herring, R. Briggs, Superficial simplicity of the 2010 El Mayor-Cucapah earthquake of Baja California in Mexico. *Nat. Geosci.* **4**, 615–618 (2011). doi:10.1038/ngeo1213

5. I. J. Hamling, S. Hreinsdóttir, K. Clark, J. Elliott, C. Liang, E. Fielding, N. Litchfield, P. Villamor, L. Wallace, T. J. Wright, E. D'Anastasio, S. Bannister, D. Burbidge, P. Denys, P. Gentle, J. Howarth, C. Mueller, N. Palmer, C. Pearson, W. Power, P. Barnes, D. J. A. Barrell, R. Van Dissen, R. Langridge, T. Little, A. Nicol, J. Pettinga, J. Rowland, M. Stirling, Complex multifault rupture during the 2016 M_w 7.8 Kaikōura earthquake, New Zealand. *Science* **356**, eaam7194 (2017). doi:10.1126/science.aam7194 Medline

6. E. Hauksson, K. Hutton, H. Kanamori, L. Jones, J. Mori, S. Hough, G. Roquemore, Preliminary Report on the 1995 Ridgecrest Earthquake Sequence in Eastern California. *Seismol. Res. Lett.* **66**, 54–60 (1995). doi:10.1785/gssrl.66.6.54

7. C. B. Amos, S. J. Brownlee, D. H. Rood, G. B. Fisher, R. Bürgmann, P. R. Renne, A. S. Jayko, Chronology of tectonic, geomorphic, and volcanic interactions and the tempo of fault slip near Little Lake, California. *GSA Bull.* **125**, 1187–1202 (2013). doi:10.1130/B30803.1

8. G. A. Davis, B. C. Burchfiel, Garlock Fault: An Intracontinental Transform Structure, Southern California. *Bull. Geol. Soc. Am.* **84**, 1407–1422 (1973). doi:10.1130/0016-7606(1973)84<1407:GFAITS>2.0.CO;2

9. Y. Fialko, M. Simons, Deformation and seismicity in the Coso geothermal area, Inyo County, California: Observations and modeling using satellite radar interferometry. *J. Geophys. Res. Solid Earth* **105** (B9), 21781–21793 (2000). doi:10.1029/2000JB900169

10. E. K. Haddon, C. B. Amos, O. Zielke, A. S. Jayko, R. Bürgmann, Surface slip during large Owens Valley earthquakes. *Geochem. Geophys. Geosyst.* **17**, 2239–2269 (2016). doi:10.1002/2015GC006033

11. Materials and methods are described in the supplementary materials.

12. S.-H. Yun, K. Hudnut, S. Owen, F. Webb, M. Simons, P. Sacco, E. Gurrola, G. Manipon, C. Liang, E. Fielding, P. Milillo, H. Hua, A. Coletta, Rapid Damage Mapping for the 2015 Mw 7.8 Gorkha Earthquake Using Synthetic Aperture Radar Data from COSMO–SkyMed and ALOS-2 Satellites. *Seismol. Res. Lett.* **86**, 1549–1556 (2015). doi:10.1785/0220150152

13. D. I. Doser, H. Kanamori, Depth of seismicity in the Imperial Valley region (1977–1983) and its relationship to heat flow, crustal structure and the October 15, 1979, earthquake. *J. Geophys. Res. Solid Earth* **91** (B1), 675–688 (1986). doi:10.1029/JB091iB01p00675

14. E. Hauksson, Crustal geophysics and seismicity in southern California. *Geophys. J. Int.* **186**, 82–98 (2011). doi:10.1111/j.1365-246X.2011.05042.x

15. N. Wetzler, T. Lay, E. E. Brodsky, H. Kanamori, Systematic deficiency of aftershocks in areas of high coseismic slip for large subduction zone earthquakes. *Sci. Adv.* **4**, eaao3225 (2018). doi:10.1126/sciadv.aao3225 Medline

16. D. P. Hill, P. A. Reasenberg, A. Michael, W. J. Arabaz, G. Beroza, D. Brumbaugh, J. N. Brune, R. Castro, S. Davis, D. Depolo, W. L. Ellsworth, J. Gomberg, S. Harmsen, L. House, S. M. Jackson, M. J. S. Johnston, L. Jones, R. Keller, S. Malone, L. Munguia, S. Nava, J. C. Pechmann, A. Sanford, R. W. Simpson, R. B. Smith, M. Stark, M. Stickney, A. Vidal, S. Walter, V. Wong, J. Zollweg, Seismicity remotely triggered by the magnitude 7.3 Landers, California, earthquake. *Science* **260**, 1617–1623 (1993). doi:10.1126/science.260.5114.1617 Medline

17. Q. Zhang, G. Lin, Z. Zhan, X. Chen, Y. Qin, S. Wdowinski, Absence of remote earthquake triggering within the Coso and Salton Sea geothermal production fields. *Geophys. Res. Lett.* **44**, 726–733 (2017). doi:10.1002/2016GL071964

18. M. Wei, D. Sandwell, Y. Fialko, R. Bilham, Slip on faults in the Imperial Valley triggered by the 4 April 2010 Mw 7.2 El Mayor-Cucapah earthquake revealed by InSAR. *Geophys. Res. Lett.* **38**, n/a (2011). doi:10.1029/2010GL045235

19. J. F. Dolan, L. J. McAuliffe, E. J. Rhodes, S. F. McGill, R. Zinke, Extreme multi-millennial slip rate variations on the Garlock fault, California: Strain super-cycles, potentially time-variable fault strength, and implications for system-level earthquake occurrence. *Earth Planet. Sci. Lett.* **446**, 123–136 (2016). doi:10.1016/j.epsl.2016.04.011

20. X. Tong, D. T. Sandwell, B. Smith-Konter, High-resolution interseismic velocity data along the San Andreas Fault from GPS and InSAR. *J. Geophys. Res. Solid Earth* **118**, 369–389 (2013). doi:10.1029/2012JB009442

21. Y. Ben-Zion, C. G. Sammis, Characterization of fault zones. *Pure Appl. Geophys.* **160**, 677–715 (2003). doi:10.1007/PL00012554

22. C. H. Scholz, *The Mechanics of Earthquakes and Faulting* (Cambridge Univ. Press, 2019).

23. S. Q. Xu, Y. Ben-Zion, Numerical and theoretical analyses of in-plane dynamic rupture on a frictional interface and off-fault yielding patterns at different scales. *Geophys. J. Int.* **193**, 304–320 (2013). doi:10.1093/gji/ggs105

24. K. W. Hudnut, L. Seeber, J. Pacheco, Cross-fault triggering in the November 1987 Superstition Hills earthquake sequence, southern California. *Geophys. Res. Lett.* **16**, 199–202 (1989). doi:10.1029/GL016i002p00199

25. W. Thatcher, D. P. Hill, Fault orientations in extensional and conjugate strike-slip environments and their implications. *Geology* **19**, 1116–1120 (1991). doi:10.1130/0091-7613(1991)019<1116:FOIEAC>2.3.CO;2

26. E. Fukuyama, Dynamic faulting on a conjugate fault system detected by near-fault tilt measurements. *Earth Planets Space* **67**, 38 (2015). doi:10.1186/s40623-015-0207-1

27. Z. E. Ross, E. Hauksson, Y. Ben-Zion, Abundant off-fault seismicity and orthogonal structures in the San Jacinto fault zone. *Sci. Adv.* **3**, e1601946 (2017). doi:10.1126/sciadv.1601946 Medline

28. Z. E. Ross, C. Rollins, E. S. Cochran, E. Hauksson, J.-P. Avouac, Y. Ben-Zion, Aftershocks driven by afterslip and fluid pressure sweeping through a fault-fracture mesh. *Geophys. Res. Lett.* **44**, 8260–8267 (2017). doi:10.1002/2017GL074634

29. L. Meng, J.-P. Ampuero, J. Stock, Z. Duputel, Y. Luo, V. C. Tsai, Earthquake in a maze: Compressional rupture branching during the 2012 M_w 8.6 Sumatra earthquake. *Science* **337**, 724–726 (2012). doi:10.1126/science.1224030 Medline

30. C. Madden Madugo, J. F. Dolan, R. D. Hartleb, New Paleoearthquake Ages from the Western Garlock Fault: Implications for Regional Earthquake Occurrence in Southern California. *Bull. Seismol. Soc. Am.* **102**, 2282–2299 (2012). doi:10.1785/0120110310

31. K. J. Kendrick, S. O. Akciz, S. J. Angster, J. Avouac, J. L. Bachhuber, S. E. Bennett, K. Blake, S. Bork, B. A. Brooks, P. Burgess, C. Chupik, T. Dawson, M. J. DeFrisco, J. Delano, S. DeLong, J. F. Dolan, C. B. DuRoss, T. Ericksen, E. Frost, R. D. Gold, N. A. Graehl, E. K. Haddon, A. E. Hatem, J. L. Hernandez, C. Hitchcock, K. W. Hudnut, R. D. Koehler, O. Kozaci, T. Ladinsky, C. M. Madugo, M. Mareschal, D. McPhillips, C. Milliner, A. E. Morelan, J. Nevitt, B. Olson, S. E. Padilla, J. R. Patton, B. Philibosian, A. Pickering, I. Pierce, D. J. Ponti, C. Pridmore, C. Rosa, N. Roth, K. M. Scharer, G. G. Seitz, E. Spangler, B. J. Swanson, K. Thomas, J. Thompson Jobe, J. A. Treiman, A. M. Williams, M. E. Oskin, Geologic observations of surface fault rupture associated with the Ridgecrest M6.4 and M7.1 earthquake sequence by the Ridgecrest Rupture Mapping Group, *Southern California Earthquake Center Annual Meeting Proceedings* (SCEC, 2019), contribution 9779.

32. SCEDC, Data are available from the Southern California Seismic Network (https://doi.org/10.7914/SN/CI), operated by the California Institute of Technology and the United States Geological Survey (2013).

33. E. Hauksson, Crustal structure and seismicity distribution adjacent to the Pacific and North America plate boundary in southern California. *J. Geophys. Res. Solid Earth* **105** (B6), 13875–13903 (2000). doi:10.1029/2000JB900016

34. F. Waldhauser, W. L. Ellsworth, A double-difference earthquake location algorithm: Method and application to the northern Hayward fault, California. *Bull. Seismol. Soc. Am.* **90**, 1353–1368 (2000). doi:10.1785/0120000006

35. Z. E. Ross, D. T. Trugman, E. Hauksson, P. M. Shearer, Searching for hidden earthquakes in Southern California. *Science* **364**, 767–771 (2019). doi:10.1126/science.aaw6888 Medline

36. D. T. Trugman, P. M. Shearer, GrowClust: A Hierarchical Clustering Algorithm for Relative Earthquake Relocation, with Application to the Spanish Springs and Sheldon, Nevada, Earthquake Sequences. *Seismol. Res. Lett.* **88** (2A), 379–391 (2017). doi:10.1785/0220160188

37. M. Kikuchi, H. Kanamori, Inversion of complex body waves. *Bull. Seismol. Soc. Am.* **81**, 2335–2350 (1991).

38. V. C. Tsai, M. Nettles, G. Ekström, A. M. Dziewonski, Multiple CMT source analysis of the 2004 Sumatra earthquake. *Geophys. Res. Lett.* **32**, (2005). doi:10.1029/2005GL023813

39. Z. Duputel, H. Kanamori, V. C. Tsai, L. Rivera, L. Meng, J.-P. Ampuero, J. M. Stock, The 2012 Sumatra great earthquake sequence. *Earth Planet. Sci. Lett.* **351–352**, 247–257 (2012). doi:10.1016/j.epsl.2012.07.017

40. Z. Zhan, H. Kanamori, V. C. Tsai, D. V. Helmberger, S. Wei, Rupture complexity of the 1994 Bolivia and 2013 Sea of Okhotsk deep earthquakes. *Earth Planet. Sci. Lett.* **385**, 89–96 (2014). doi:10.1016/j.epsl.2013.10.028

41. Q. Shi, S. Wei, M. Chen, An MCMC multiple point sources inversion scheme and its application to the 2016 Kumamoto Mw 6.2 earthquake. *Geophys. J. Int.* **215**, 737–752 (2018). doi:10.1093/gji/ggy302

42. Z. Zhan, H. Kanamori, Recurring large deep earthquakes in Hindu Kush driven by a sinking slab. *Geophys. Res. Lett.* **43**, 7433–7441 (2016). doi:10.1002/2016GL069603

43. T. Bodin, M. Sambridge, Seismic tomography with the reversible jump algorithm. *Geophys. J. Int.* **178**, 1411–1436 (2009). doi:10.1111/j.1365-246X.2009.04226.x

44. S. E. Minson, D. S. Dreger, Stable inversions for complete moment tensors. *Geophys. J. Int.* **174**, 585–592 (2008). doi:10.1111/j.1365-246X.2008.03797.x

45. M.-A. Meier, J. P. Ampuero, T. H. Heaton, The hidden simplicity of subduction megathrust earthquakes. *Science* **357**, 1277–1281 (2017). doi:10.1126/science.aan5643 Medline

46. L. Zhu, L. A. Rivera, A note on the dynamic and static displacements from a point source in multilayered media. *Geophys. J. Int.* **148**, 619–627 (2002). doi:10.1046/j.1365-246X.2002.01610.x

47. J. Mori, D. Helmberger, Large-amplitude Moho reflections (SmS) from Landers aftershocks, southern California. *Bull. Seismol. Soc. Am.* **86**, 1845–1852 (1996).

48. B. L. N. Kennett, E. R. Engdahl, Traveltimes for global earthquake location and phase identification. *Geophys. J. Int.* **105**, 429–465 (1991). doi:10.1111/j.1365-246X.1991.tb06724.x

49. J. F. Zumberge, M. B. Heflin, D. C. Jefferson, M. M. Watkins, F. H. Webb, Precise point positioning for the efficient and robust analysis of GPS data from large networks. *J. Geophys. Res. Solid Earth* **102** , 5005–5017 (1997). doi:10.1029/96JB03860

50. W. Bertiger, S. D. Desai, B. Haines, N. Harvey, A. W. Moore, S. Owen, J. P. Weiss, Single receiver phase ambiguity resolution with GPS data. *J. Geod.* **84**, 327–337 (2010). doi:10.1007/s00190-010-0371-9

51. Z. Liu, S. Owen, A. Moore, Rapid Estimate and Modeling of Permanent Coseismic Displacements for Large Earthquakes Using High-Rate Global Positioning System Data. *Seismol. Res. Lett.* **85**, 284–294 (2014). doi:10.1785/0220130174

52. C. Liang, Z. Liu, E. J. Fielding, R. Bürgmann, InSAR Time Series Analysis of L-Band Wide-Swath SAR Data Acquired by ALOS-2. *IEEE Trans. Geosci. Remote Sens.* **56**, 4492–4506 (2018). doi:10.1109/TGRS.2018.2821150

53. P. A. Rosen, E. Gurrola, G. F. Sacco, H. Zebker, in *9th European Conference on Synthetic Aperture Radar* (EUSAR, 2012), pp. 730–733.

54. C. W. Chen, H. A. Zebker, Phase unwrapping for large SAR interferograms: Statistical segmentation and generalized network models. *IEEE Trans. Geosci. Remote Sens.* **40**, 1709–1719 (2002). doi:10.1109/TGRS.2002.802453

55. I. Joughin, Ice-sheet velocity mapping: A combined interferometric and speckle-tracking approach. *Ann. Glaciol.* **34**, 195–201 (2002). doi:10.3189/172756402781817978

56. R. B. Lohman, M. Simons, Some thoughts on the use of InSAR data to constrain models of surface deformation: Noise structure and data downsampling. *Geochem. Geophys. Geosyst.* **6**, n/a (2005). doi:10.1029/2004GC000841

57. Z. Duputel, P. S. Agram, M. Simons, S. E. Minson, J. L. Beck, Accounting for prediction uncertainty when inferring subsurface fault slip. *Geophys. J. Int.* **197**, 464–482 (2014). doi:10.1093/gji/ggt517

58. R. Jolivet, Z. Duputel, B. Riel, M. Simons, L. Rivera, S. E. Minson, H. Zhang, M. G. Aivazis, F. Ayoub, S. Leprince, S. Samsonov, M. Motagh, E. J. Fielding, The 2013 Mw 7.7 Balochistan Earthquake: Seismic Potential of an Accretionary Wedge. *Bull. Seismol. Soc. Am.* **104**, 1020–1030 (2014). doi:10.1785/0120130313

59. Z. Duputel, J. Jiang, R. Jolivet, M. Simons, L. Rivera, J.-P. Ampuero, B. Riel, S. E. Owen, A. W. Moore, S. V. Samsonov, F. Ortega Culaciati, S. E. Minson, The Iquique earthquake sequence of April 2014: Bayesian modeling accounting for prediction uncertainty. *Geophys. Res. Lett.* **42**, 7949–7957 (2015). doi:10.1002/2015GL065402

60. S. E. Minson, M. Simons, J. L. Beck, Bayesian inversion for finite fault earthquake source models I—Theory and algorithm. *Geophys. J. Int.* **194**, 1701–1726 (2013). doi:10.1093/gji/ggt180

61. E. J. Fielding, S. S. Sangha, D. P. Bekaert, S. V. Samsonov, J. C. Chang, Surface deformation of north-central Oklahoma related to the 2016 Mw 5.8 Pawnee earthquake from SAR interferometry time series. *Seismol. Res. Lett.* **88**, 971–982 (2017). doi:10.1785/0220170010